

Development of liquid-environment frequency modulation atomic force microscope with low noise deflection sensor for cantilevers of various dimensions

Takeshi Fukuma^{a)} and Suzanne P. Jarvis

Centre for Research on Adaptive Nanostructures and Nanodevices, Lincoln Place Gate, Trinity College Dublin, Dublin 2, Ireland

(Received 27 January 2005; accepted 27 February 2006; published online 3 April 2006)

We have developed a liquid-environment frequency modulation atomic force microscope (FM-AFM) with a low noise deflection sensor for a wide range of cantilevers with different dimensions. A simple yet accurate equation describing the theoretical limit of the optical beam deflection method in air and liquid is presented. Based on the equation, we have designed a low noise deflection sensor. Replaceable microscope objective lenses are utilized for providing a high magnification optical view (resolution: $<3 \mu\text{m}$) as well as for focusing a laser beam (laser spot size: $\sim 10 \mu\text{m}$). Even for a broad range of cantilevers with lengths from 35 to 125 μm , the sensor provides deflection noise densities of less than 11 $\text{fm}/\sqrt{\text{Hz}}$ in air and 16 $\text{fm}/\sqrt{\text{Hz}}$ in water. In particular, a cantilever with a length of 50 μm gives the minimum deflection noise density of 5.7 $\text{fm}/\sqrt{\text{Hz}}$ in air and 7.3 $\text{fm}/\sqrt{\text{Hz}}$ in water. True atomic resolution of the developed FM-AFM is demonstrated by imaging mica in water. © 2006 American Institute of Physics.
[DOI: 10.1063/1.2188867]

I. INTRODUCTION

Subnanometer resolution of frequency modulation atomic force microscopy¹ (FM-AFM) has been demonstrated on various surfaces.^{2,3} Until recently, however, the high spatial resolution of FM-AFM was available only in ultrahigh vacuum environments. This limitation has prevented a wide range of applications in air and liquids.^{4,5} Recently, Fukuma *et al.* presented a way to overcome this limitation.^{6–8} They demonstrated true molecular resolution of FM-AFM in air⁶ and liquid.⁷ Furthermore, true atomic resolution of FM-AFM in liquid was also demonstrated.⁸

The main improvement that brought the success was the reduction of noise from the cantilever deflection sensor.⁹ The reported deflection noise densities measured in air and water were 17 and 40 $\text{fm}/\sqrt{\text{Hz}}$, respectively, whereas typical values are in the range of 100–1000 $\text{fm}/\sqrt{\text{Hz}}$ in air.¹⁰ The low deflection noise makes it possible to obtain the maximum signal-to-noise ratio (SNR) that is limited only by the thermal vibration of the cantilever. A clean deflection signal is also essential for a stable cantilever self-oscillation with a small oscillation amplitude (typically less than 1 nm). A small amplitude has been proven to be a great advantage for increasing the sensitivity to short-range interaction forces and thereby obtaining a high spatial resolution.^{11–13}

The use of smaller cantilevers^{14–19} with a higher resonance frequency has recently attracted much attention due to their potential to improve the sensitivity and time response in FM-AFM techniques.^{1,20} The development of a low noise deflection sensor for small cantilevers is therefore of great importance. On the other hand, different types of cantilevers

with various dimensions are used in AFM experiments for different purposes and different operation modes. Thus, the applicability to a wide range of cantilevers with different dimensions is also important.

Deflection sensors for small cantilevers have been developed using interferometry^{17,19} and optical beam deflection (OBD) methods.^{14–16,18} We prefer to use the OBD method because of its simple experimental setup and easy optical beam alignment. More importantly, the OBD method can be easily combined with high magnification optical microscope which is particularly useful for biological applications. The previously reported OBD sensors for small cantilevers utilized a focus lens with a high numerical aperture (NA) for obtaining a small laser spot as well as for collecting the reflected laser beam. This design allows one to place a position sensitive photodetector (PSPD) far away from the cantilever without any loss of laser power. The main drawback of this design is the large divergence of focused laser beam which deteriorates the deflection sensitivity. This is partially compensated by the use of short cantilevers because a shorter cantilever gives a higher deflection sensitivity in the OBD method. However, the sensor does not perform very well with larger cantilevers.

The present work aims at developing an FM-AFM with a low noise deflection sensor which is applicable to a wide range of cantilevers with different dimensions. In addition, the AFM also features high magnification optical view for easy alignment of the laser beam and tip positioning over the sample. In this article, we discuss the theoretical limit of the OBD method with special attention to the liquid environment. The design and performance of our AFM are discussed

^{a)}Electronic mail: takeshi.fukuma@tcd.ie

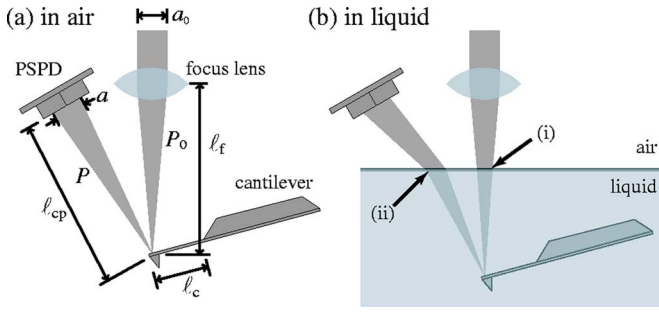


FIG. 1. (Color online) Typical experimental setup for a cantilever deflection sensor using the OBD method (a) in air and (b) in liquid.

in comparison with the expected theoretical limit. True atomic resolution of our AFM in liquid is demonstrated by imaging mica in water.

II. THEORETICAL LIMIT OF THE OBD METHOD

A. Deflection sensitivity

Figure 1 shows a typical experimental setup for a cantilever deflection sensor using the OBD method. A cantilever displacement Δz induces a cantilever deflection. This in turn gives rise to a displacement of the laser spot on a PSPD (Δa) which is given by²¹

$$\Delta a = 3 \frac{\ell_{cp}}{\ell_c} \Delta z, \quad (1)$$

where ℓ_{cp} and ℓ_c are the distance from the cantilever backside to the PSPD and cantilever length, respectively.

The displacement of the laser spot results in a difference between the photoinduced currents (Δi) from the two photodiodes consisting of the PSPD. Assuming that the laser spot shape is rectangular and the power distribution is uniform, the current difference Δi_1 is described by

$$\Delta i_1 = \eta P \frac{2}{a} \Delta a, \quad (2)$$

where η , P , and a are efficiency of the light-to-current conversion at the photodiode, total power of the laser beam irradiated onto the PSPD, and diameter of the laser spot on the PSPD, respectively. On the other hand, when we assume that the laser beam has a Gaussian distribution with a standard deviation of σ , the current difference Δi_2 is given by

$$\Delta i_2 = 4 \eta P \frac{1}{2\pi\sigma^2} \int_0^{\Delta a} \int_0^{d/2} \exp\left(-\frac{x^2 + y^2}{2\sigma^2}\right) dx dy, \quad (3)$$

where d is the width of the active area of the PSPD.

Equation (2) is more simple and intuitive than Eq. (3) whereas Eq. (3) is more accurate. To obtain an intuitive and accurate expression, here we introduce a coefficient χ which is given by $\chi = \Delta i_2 / \Delta i_1$. The value for χ is almost constant in most of the designs for OBD sensors. In our design, the variation of χ is less than 0.3% with the Δz range of ± 10 nm. If we define a as a diameter of beam cross section at $1/e$ (or $1/e^2$) of maximum laser intensity, the coefficient χ will be 1.13 (or 1.60). With this coefficient and Eqs. (1) and (2), the current difference Δi is given by

$$\Delta i = 6\chi\eta P \frac{\ell_{cp}}{\ell_{ca}} \Delta z. \quad (4)$$

Although Eq. (4) is accurate, it has some drawbacks in practice. The laser power P is usually difficult to measure in actual deflection sensors while the laser power irradiated onto the cantilever (P_0) is often easy to measure. With an attenuation factor of α , P is described as $P = \alpha P_0$. Equation (4) implies that Δi increases with increasing ℓ_{cp} . However, this is incorrect because a changes depending on ℓ_{cp} as described by the following equation:

$$a = \frac{\ell_{cp}}{\ell_f} a_0, \quad (5)$$

where a_0 and ℓ_f are the diameter of the collimated laser beam and the focal length of the focus lens. Therefore, Eq. (4) is rewritten as

$$\Delta i = 6\chi\eta\alpha \frac{P_0 \ell_f}{a_0 \ell_c} \Delta z. \quad (6)$$

From this equation, the sensitivity of the deflection signal to the tip displacement (S_z) is given by

$$S_z = 6\chi\eta\alpha R_{IV} A_{diff} \frac{P_0 \ell_f}{a_0 \ell_c}, \quad (7)$$

where R_{IV} and A_{diff} are the transimpedance of the I - V converter and the gain of the differential amplifier, respectively. This equation shows that S_z is independent of ℓ_{cp} .

In the case of liquid-environment AFMs, the influence of laser beam reflection and refraction at the liquid/air interface has to be taken into account. The reflection results in a loss of laser power, leading to a lower α value. The refraction generally enhances S_z as explained below. The relationship between the incident and refracted laser beams at an interface is described by Snell's law,

$$n_i \sin \theta_i = n_r \sin \theta_r. \quad (8)$$

θ_i and θ_r are the incident and refracting angles of the light, respectively. n_i and n_r are the refractive indices of the media for the incident and refracted lights, respectively. From Eq. (8), $d\theta_r / d\theta_i$ [$\equiv D(\theta_i)$] is given by

$$D(\theta_i) \equiv \frac{d\theta_r}{d\theta_i} = \frac{\cos \theta_i}{\sqrt{(n_r/n_i)^2 - \sin^2 \theta_i}}. \quad (9)$$

At the air-to-liquid interface [(i) in Fig. 1(b)], the beam divergence is reduced approximately by $D(0) = n_i/n_r$. Assuming that the refractive indices of air and liquid are 1 and n_ℓ , respectively, $D(0) = 1/n_\ell$. Thus, S_z is enhanced by n_ℓ . If the liquid is water with a refractive index of 1.33, S_z is enhanced by 33%. At the liquid-to-air interface [(ii) in Fig. 1(b)], the laser beam divergence is enhanced approximately by $D(2\theta_t)$, where θ_t is the tilt angle of the cantilever. For example, if $\theta_t = 15^\circ$ and the liquid is water, the laser beam divergence is enhanced by 54%. However, the refraction also enhances the deflection of the laser beam by the same factor. Consequently, the refraction at the liquid-to-air interface does not affect S_z . Therefore, S_z in liquid is larger than that in air by a

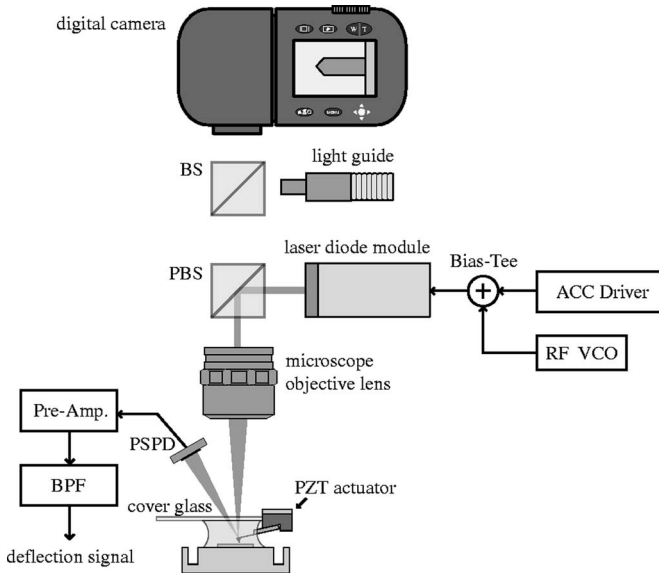


FIG. 2. Schematic drawing of the experimental setup for the developed cantilever deflection sensor using the OBD method.

factor of n_ℓ . Since the refractive index of air is approximately 1, a general description of S_z , which is valid both in air and liquid, is given by

$$S_z = 6\chi\eta\alpha n_m R_{IV} A_{\text{diff}} \frac{P_0 \ell_f}{a_0 \ell_c}, \quad (10)$$

where n_m is the refractive index of the medium of the operating environment.

B. Photodiode shot noise limit

The major noise sources in the OBD method include photodiode shot noise, load resistance Johnson noise, and laser beam intensity fluctuation and mode hopping.^{9,21} Among them, the photodiode shot noise usually determines the lower limit of the deflection noise density (n_z). The voltage noise density of the deflection signal (n_v) arising from the photodiode shot noise is given by

$$n_v = R_{IV} A_{\text{diff}} \sqrt{2e\eta\alpha P_0}, \quad (11)$$

where e is an electron charge. From this equation and Eq. (10), n_z is given by

$$n_z = \frac{a_0 \ell_c}{6\chi n_m \ell_f} \sqrt{\frac{2e}{\eta\alpha P_0}}. \quad (12)$$

This equation shows the theoretical limit of the noise performance obtained by the OBD method. The equation contains only independent parameters and hence gives us a direct guideline for reducing n_z . Namely, increasing ℓ_f , α , and P_0 , and decreasing a_0 and ℓ_c will improve the noise performance of an OBD sensor.

III. DESIGN OF THE DEFLECTION SENSOR

Figure 2 shows a schematic drawing of the experimental setup for the developed deflection sensor. In this section, key design features which determine the performance of the deflection sensor are described in detail.

A. High quality laser beam source

The fine focusing of a laser beam requires a high quality collimated laser beam. The laser beam should have a circular cross section, a small aberration, and a small divergence. To satisfy these requirements, a large a_0 is desirable. On the other hand, Eq. (12) shows that a smaller a_0 is desirable for obtaining a lower n_z . A smaller a_0 also helps in designing a compact deflection sensor. Thus, we have to choose a laser beam source which produces a high quality collimated laser beam with a small a_0 .

Using a single mode fiber is the easiest way to obtain a high quality laser beam. However, this design generally gives a large n_z due to the large laser intensity fluctuation caused by the reflection at the fiber end. Hence, the design is rarely adopted in OBD sensors. The combination of a laser diode and an aspheric collimation lens is the most commonly used design. Although the laser beam produced by the optics has a low intensity noise, it has an elliptic cross section and a large astigmatism. This results in a poor focusing at the cantilever backside.

In our deflection sensor, we used a commercially available laser diode module (VHK-4.9 mW-635 nm: Edmund Optics) with some modifications. The module produces a laser beam with a wavelength of 635 nm, a_0 of 1.1 mm, and divergence angle of 0.7 mrad. A microcylindrical lens integrated in the laser diode package corrects most of the aberration and asymmetry of the laser beam without increasing the size of the optical system. The lens also reduces the divergence angle of the emitted laser beam from the diode chip. This facilitates in the collection of all the light with a collimation lens and to keep a_0 as small as possible.

The laser diode module comes with an automatic power constant (APC) driver circuit. We replaced it with a home-built automatic current constant (ACC) laser driver circuit with a radio frequency (rf) modulation function. A 300 MHz modulation signal generated by a voltage controlled oscillator (VCO) (Mini-Circuits: POS-400) is added to a dc driving current produced by an ACC driver circuit (ThorLabs: IP500) using a bias tee (Mini-Circuits: PBTC-1GW). The rf laser power modulation reduces the coherence of the laser beam. This is remarkably effective at reducing optical feedback noise and interference noise as reported previously.⁹

B. Replaceable microscope objective lenses

The fine focusing of a laser beam requires a focus lens with a high NA, which usually has a short ℓ_f . However, Eq. (12) shows that a long ℓ_f is desirable for obtaining a low n_z . These two requirements make it difficult to design a low noise OBD sensor for cantilevers with different dimensions.

In our deflection sensor, we used two replaceable microscope objective lenses for focusing a laser beam as well as for providing a high magnification optical view. The illumination light is transmitted through a beam splitter (BS) and the objective lens. The reflected light is collected with a digital camera (Nikon: COOLPIX 4500) which forms an optical image. The collimated laser beam is transmitted through a polarizing beam splitter (PBS) and focused with the objective lens.

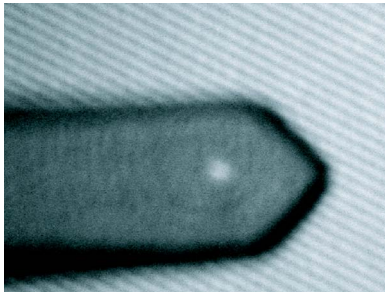


FIG. 3. (Color online) An optical image of a cantilever and a grating taken with the $\times 20$ lens. The width of the cantilever backside is about $37 \mu\text{m}$. The pitch and the height of the grating are $3 \mu\text{m}$ and 20 nm , respectively. The bright spot on the cantilever is a laser spot focused with the objective lens. Note that the focus is on the grating and hence the cantilever and the laser spot are slightly out of focus.

The two replaceable lenses include $\times 5$ (Nikon: CF IC EPI Plan $5\times$) and $\times 20$ (Nikon: CF IC EPI Plan SLWD $20\times$) lenses. The $\times 5$ lens with a low NA (0.13) and a long ℓ_f (40 mm) gives a lower n_z provided that the laser spot size (about $25 \mu\text{m}$) is comparable to the size of the cantilever backside. The $\times 20$ lens with a high NA (0.35) and a short ℓ_f (10 mm) provides a small laser spot size (about $10 \mu\text{m}$) and a high magnification optical view. Thus, the $\times 20$ lens is useful for small cantilevers or precise cantilever alignment over large biological samples. The two lenses have the same parfocal length of 45 mm and similar working distances (WDs): 22.5 and 20.5 mm for the $\times 5$ and $\times 20$ lenses, respectively. Therefore, these two lenses are replaceable without modifying any other parts of the system.

Figure 3 shows an optical image of a cantilever (Nanosensors: NCH) and a grating (MikroMasch: TGZ01) taken with the $\times 20$ lens. The image shows the stripes corresponding to the grating pattern with a pitch of $3 \mu\text{m}$ and a step height of 20 nm . This reveals that the optical view provided by the $\times 20$ lens has a resolution better than $3 \mu\text{m}$. The image also demonstrates that the laser spot size is much smaller than that obtained with conventional AFMs.²² The high magnification optical view facilitates the alignment of the laser spot over the cantilever backside as well as tip positioning over the sample.

C. High efficiency photodetector

A laser beam focused with a high NA objective lens has a large divergence angle. The PSPD has to be placed close to the cantilever to minimize the laser power loss. A large active area of the PSPD is desirable for collecting all the reflected light whereas the size of the PSPD has to be small enough to be placed close to the cantilever. In general, a focus lens with a high NA has a relatively short WD. This makes it difficult to place the PSPD close to the cantilever.

The PSPD used in our sensor is four-segment Si PIN photodiode (Hamamatsu Photonics: S6695-01) with a package size of $4 \times 4.8 \times 1.8 \text{ mm}^3$. This small package and the long WD of the microscope objective lenses ($>20 \text{ mm}$) allow us to place the PSPD in the space between the lens and the cantilever, as shown in Fig. 2. The short ℓ_{cp} of 17 mm

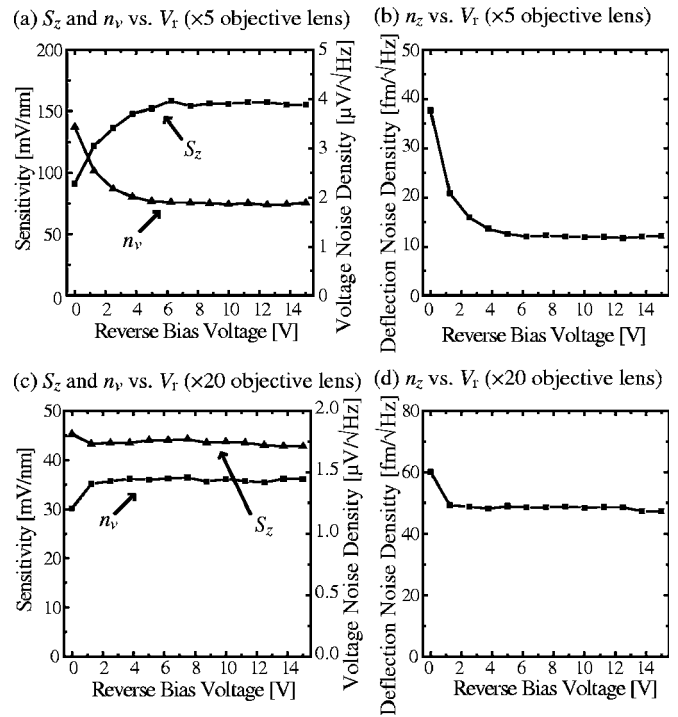


FIG. 4. V_r dependence of S_z and n_v measured with (a) the $\times 5$ and (c) the $\times 20$ lenses. V_r dependence of n_z measured with (b) the $\times 5$ and (d) the $\times 20$ lenses. The measurements were performed in air. The cantilever used was NCHR from Nanosensors.

makes it possible to keep a smaller than the size of the PSPD active area ($2 \times 2 \text{ mm}^2$) even with the $\times 20$ lens ($a = 1.88 \text{ mm}$).

For the $\times 5$ lens, $a = 0.47 \text{ mm}$, which is much smaller than that in conventional AFMs.¹⁰ A high efficiency light-to-current conversion with such a small laser spot imposes additional requirements on the PSPD specifications and its operating conditions. First, the gap distance between the photodiode segments has to be much smaller than a to avoid laser power loss and a resultant sensitivity decrease. The PSPD used in our sensor has a relatively small gap distance of $15 \mu\text{m}$ which is more than 30 times smaller than a . Thus, the influence is negligible in our sensor. Secondly, a high intensity laser beam irradiated onto a small area induces the saturation of photoinduced charges. This leads to a decrease of S_z and an increase in the shot noise. These two effects together result in a significant increase of n_z .

Applying a reverse bias voltage V_r across the photodiode is effective for enhancing the drift of the photoinduced charges and thereby preventing their saturation. Figure 4 shows V_r dependence of S_z , n_v , and n_z measured with the $\times 5$ and the $\times 20$ lenses. For the $\times 5$ lens, S_z increases and n_v decreases with increasing V_r [Fig. 4(a)]. Consequently, n_z is dramatically reduced with increasing V_r [Fig. 4(b)]. For the $\times 20$ lens, the influence of V_r is not as significant as that with the $\times 5$ lens because of the large a . In our deflection sensor, V_r is usually set to 9 V.

IV. PERFORMANCE OF THE DEFLECTION SENSOR

In this section, the performance of the developed deflection sensor is discussed in comparison with the theoretical

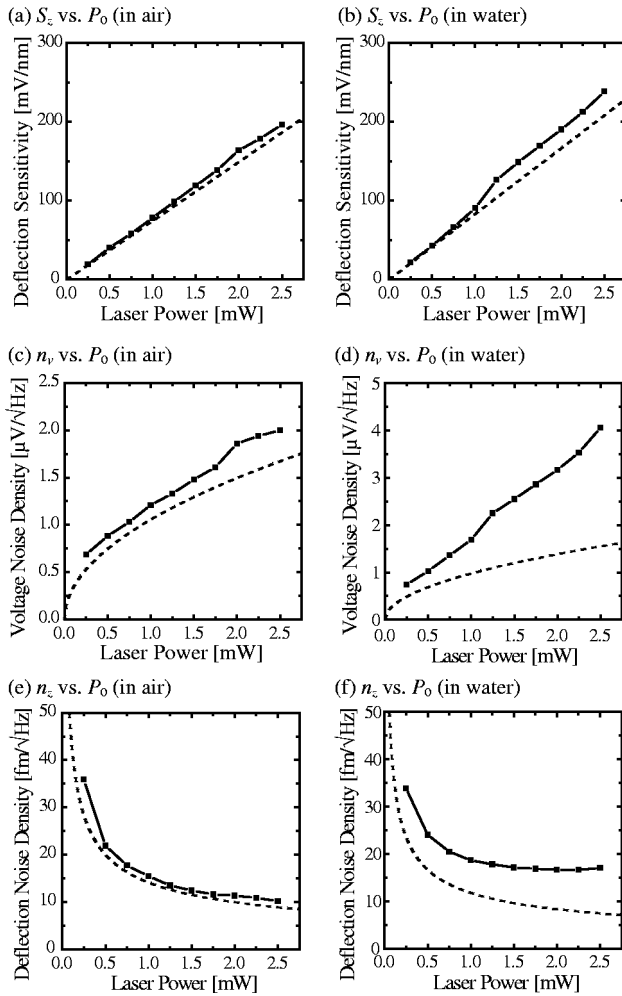


FIG. 5. P_0 dependences of [(a) and (b)] S_z , [(c) and (d)] n_v , and [(e) and (f)] n_z . The data shown in (a), (c), and (e) were measured in air while those in (b), (d), and (f) were measured in water. The measurements were performed with the $\times 5$ lens. The cantilever used was NCHR from Nanosensors. The solid lines show experimentally measured values while the dotted lines show theoretically calculated values with Eq. (10) for (a) and (b), Eq. (11) for (c) and (d), and Eq. (12) for (e) and (f). The parameters used in the calculations are given below. $\chi=1.13$. $\eta=0.48$ A/W. $n_m=1$ (in air) or 1.33 (in water). $\alpha=0.73$ (in air) or 0.63 (in water). $R_{IV}=10$ k Ω . $A_{\text{diff}}=10$. $\ell_f=40$ mm. $a_0=1.1$ mm. $\ell_c=115$ μ m.

expectations from the shot noise limit given by Eq. (12). Applicability to a wide range of cantilevers having different dimensions is also discussed.

A. Laser power dependence

Figure 5 shows P_0 dependences of S_z , n_v , and n_z measured in air and water. The solid lines show the experimentally measured values while the dotted lines show theoretically calculated values from Eqs. (10)–(12). All the results obtained in air show good agreements with theoretical expectations. This demonstrates that our deflection sensor has shot noise limited performance. For the liquid environment, S_z shows good agreement with the shot noise limit while the others do not. n_v shows an almost linear dependence on P_0 and hence n_z is almost constant at laser powers higher than 1 mW. This suggests that the noise performance in liquid is limited by noise from the laser beam. The laser beam reflected at the cover glass partially goes back to the laser

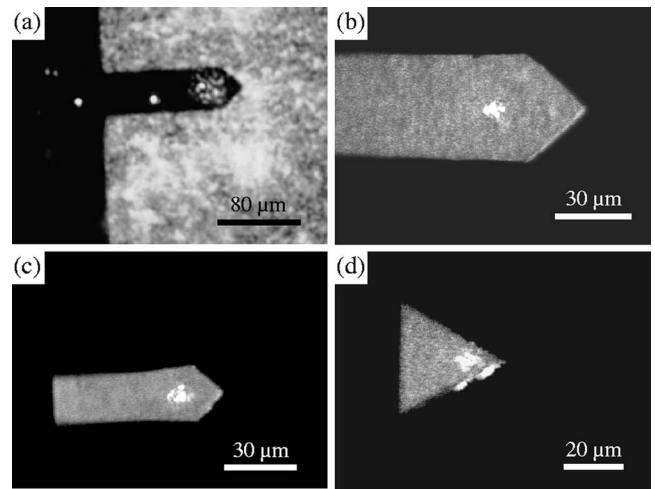


FIG. 6. Optical images of cantilevers having different dimensions. [(a) and (b)] NCHR: $\ell_c=125$ μ m, $w_c=30$ μ m, $t_c=4$ μ m. (c) NCVH: $\ell_c=50$ μ m, $w_c=30$ μ m, $t_c=1.8$ μ m. (d) Arrow UHF (type C): $\ell_c=35$ μ m, $w_c=0-42$ μ m, $t_c=1$ μ m. The dimensions described above are nominal values provided by the manufacturer (Nanosensors). The $\times 5$ lens was used for taking the image (a) while the others were taken with the $\times 20$ lens.

diode chip. This induces a mode hop noise referred to as optical feedback noise. The rf laser power modulation significantly reduces this noise but not perfectly.⁹ Therefore, the laser mode hop noise is likely to exceed the shot noise at a high laser output power. The use of an optical window with an antireflection coating may help us to reduce the noise level to the shot noise limit in future. The laser power is usually set to 2 mW in our deflection sensor.

B. High magnification optics

Cantilevers used in FM-AFM have relatively large spring constants (typically 10–50 N/m) in an effort to minimize instabilities. We have chosen three types of cantilevers with different dimensions for this study. Those cantilevers have nearly the same spring constant ranging from 20 to 40 N/m while their resonance frequencies and dimensions are very different. Figure 6 shows optical images of those cantilevers taken with the digital camera integrated in the AFM system. The geometrical parameters of the cantilevers such as ℓ_c , width (w_c), and thickness (t_c) are given in the figure caption.

For the $\times 5$ lens, the laser spot size on the cantilever backside is about 25 μ m. This is small enough for most of the commercially available AFM cantilevers, which have a width of wider than 30 μ m. The cantilever is tilted by 15° so that the illumination light reflected at the cantilever is not collected by the $\times 5$ lens having a small NA. Consequently, the cantilever is imaged as a black shadow, as shown in Fig. 6(a). For the $\times 20$ lens, the large NA makes it possible to collect some of the light reflected at the cantilever backside. Thus, the cantilever is imaged with a bright contrast, as shown in Fig. 6(b). The laser spot size obtained with the $\times 20$ lens is about 10 μ m, which is even smaller than the size of the small cantilevers [Figs. 6(c) and 6(d)]. Thus, we expect that the sensor is applicable to the cantilevers shorter than 35 μ m.

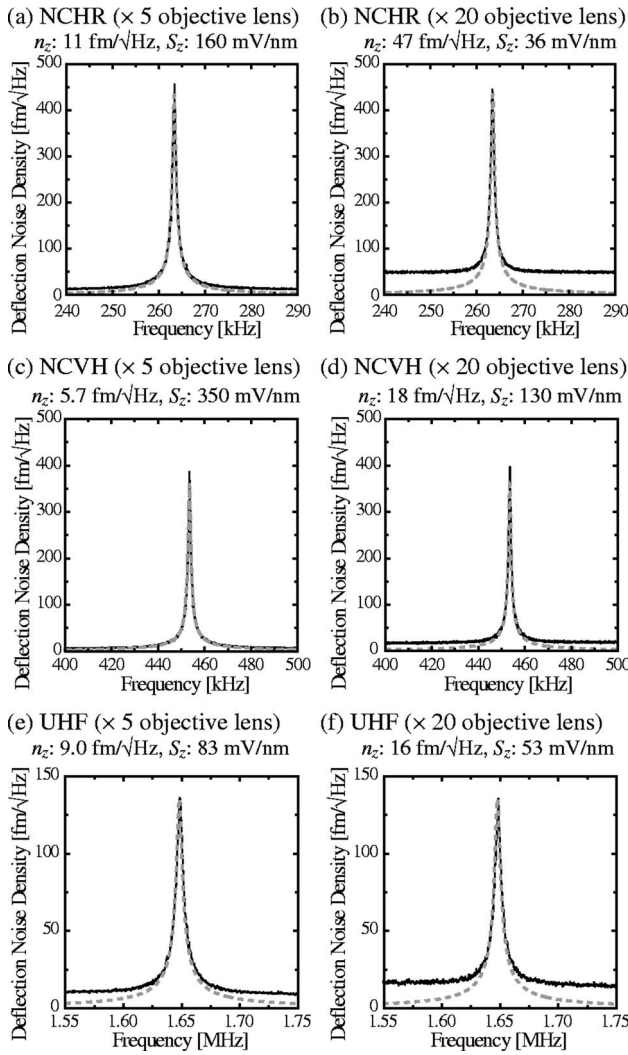


FIG. 7. Frequency spectra of cantilever thermal Brownian motion measured with different cantilevers and different objective lenses in air. The black lines show experimentally measured values while the dotted lines show theoretically calculated values for thermal Brownian motion with Eq. (13). [(a) and (b)] NCHR: $k=21$ N/m, $f_0=263$ kHz, $Q=396$, Al backside coating. [(c) and (d)] NCVH: $k=21.5$ N/m, $f_0=454$ kHz, $Q=485$, Au backside coating. [(e) and (f)] Arrow UHF (type C): $k=31$ N/m, $f_0=1.66$ MHz, $Q=358$, Al backside coating. The Au backside coating of NCVH was added to keep the measurements consistent.

C. Q -limited noise performance

The noise in the deflection signal includes noise arising from the deflection sensor and the thermal Brownian vibration of the cantilever. The sensor noise has to be less than the thermal noise in order to obtain thermal-noise-limited (Q -limited) noise performance. The spectral noise density of the cantilever thermal Brownian motion (n_{zB}) is given by

$$n_{zB} = \sqrt{\frac{2k_B T}{\pi f_0 k Q} \frac{1}{[1 - (f/f_0)^2]^2 + [f/(f_0 Q)]^2}}, \quad (13)$$

where f , f_0 , and k are vibration frequency, resonance frequency, and spring constant of the cantilever, respectively. k_B and T are Boltzmann constant and absolute temperature, respectively.

Figures 7 and 8 show frequency spectra of cantilever thermal Brownian motion measured with different cantile-

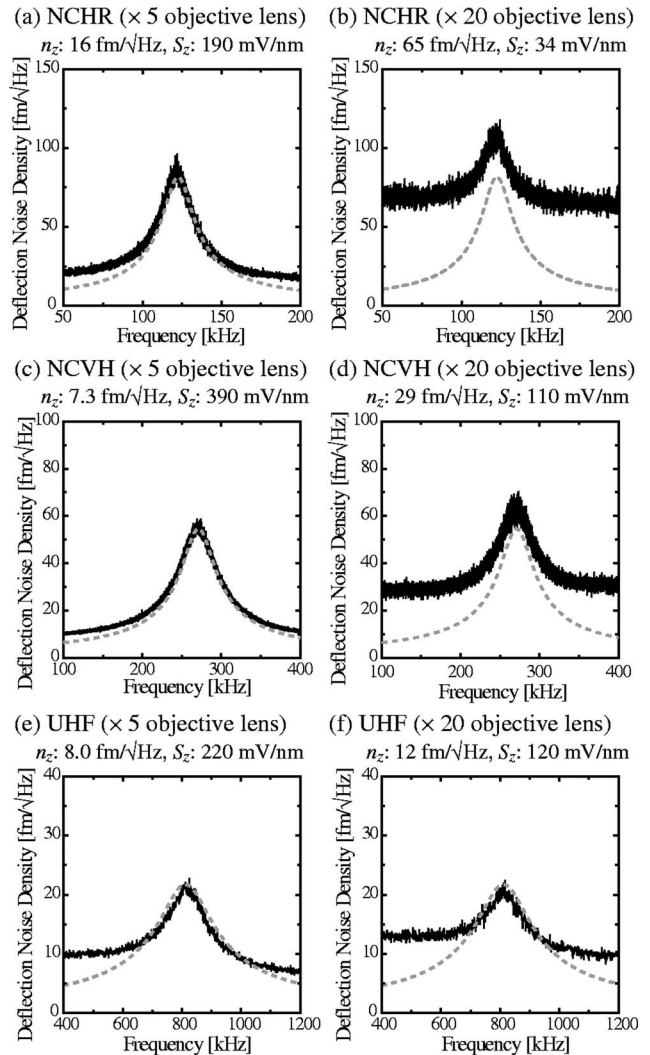


FIG. 8. Frequency spectra of cantilever thermal Brownian motion measured with different cantilevers and different objective lenses in water. The black lines show experimentally measured values while the dotted lines show theoretically calculated values for thermal Brownian motion with Eq. (13). [(a) and (b)] NCHR: $k=21$ N/m, $f_0=123$ kHz, $Q=6.5$, Al backside coating. [(c) and (d)] NCVH: $k=21.5$ N/m, $f_0=271$ kHz, $Q=6.6$, Au backside coating. [(e) and (f)] Arrow UHF (type C): $k=31$ N/m, $f_0=812$ kHz, $Q=4.5$, Al backside coating. The Au backside coating of NCVH was added to keep the measurements consistent.

vers and different objective lenses. The measurements were performed both in air (Fig. 7) and in water (Fig. 8). The black lines show experimentally measured values while the dotted lines show theoretically calculated values for thermal Brownian motion with Eq. (13). The difference between the solid and dotted lines around the resonance frequency shows the influence of the sensor noise on the FM-AFM measurements. The deflection noise densities obtained from those spectra are plotted as a function of cantilever length in Fig. 9.

The thermal noise peak at the cantilever resonance in air is relatively high due to the high Q factor. This makes it easier to achieve Q -limited noise performance. In fact, Fig. 7 shows that the sensor noise is negligible compared to the thermal noise around the cantilever resonance in all the cases. The thermal noise peak becomes lower as the resonance frequency becomes higher [see Eq. (13)]. For example, Figs. 7(e) and 7(f) show that the thermal peak of the

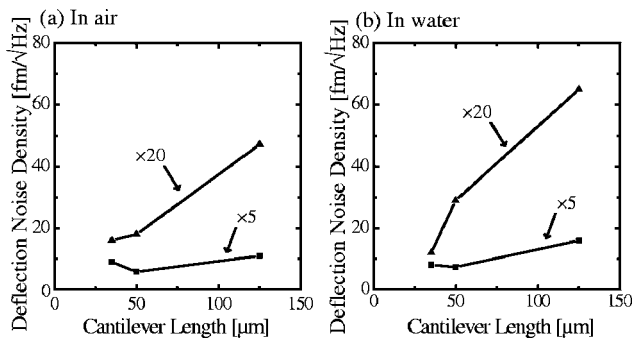


FIG. 9. ℓ_c dependence of n_z measured (a) in air and (b) in water with the $\times 5$ and $\times 20$ lenses.

UHF cantilever is about $130 \text{ fm}/\sqrt{\text{Hz}}$ in air, which is much lower than that for NCH ($450 \text{ fm}/\sqrt{\text{Hz}}$). Since the typical n_z for conventional AFMs (Ref. 10) is in the range of $100\text{--}1000 \text{ fm}/\sqrt{\text{Hz}}$, Q -limited noise performance is not easy to achieve with the UHF cantilever. Nevertheless, the low n_z of our sensor, $9.0 \text{ fm}/\sqrt{\text{Hz}}$ for the $\times 5$ lens and $16 \text{ fm}/\sqrt{\text{Hz}}$ for the $\times 20$ lens, makes it possible to obtain Q -limited noise performance even with such a high frequency cantilever.

The Q factor in liquid is much lower than that in air. This makes it more difficult to achieve Q -limited noise performance. For example, n_z at the thermal peaks is $80 \text{ fm}/\sqrt{\text{Hz}}$ for the NCHR cantilever, $55 \text{ fm}/\sqrt{\text{Hz}}$ for the NCVH cantilever, and $20 \text{ fm}/\sqrt{\text{Hz}}$ for the UHF cantilever. Those values are well below the typical n_z values for conventional AFMs (Ref. 10) and therefore the FM-AFM performance is usually limited by the sensor noise. For our deflection sensor, it is still possible to achieve Q -limited noise performance with all the cantilevers even in liquid environments, as shown in Fig. 8. The figure shows that the $\times 5$ lens provides Q -limited noise performance for all the cantilevers while the $\times 20$ lens does only for the UHF cantilever. Thus, the $\times 20$ lens should be used only with small cantilevers unless high magnification optical view is required.

Figure 9 shows that our deflection sensor with the $\times 5$ lens provides n_z of less than $16 \text{ fm}/\sqrt{\text{Hz}}$ irrespective of cantilever dimensions and environments. In particular, the combination of NCVH cantilever and the $\times 5$ lens provides the lowest n_z : $5.7 \text{ fm}/\sqrt{\text{Hz}}$ in air and $7.3 \text{ fm}/\sqrt{\text{Hz}}$ in water. With the NCHR and NCVH cantilevers, the $\times 5$ lens gives 3.2–4.3 times lower n_z than the $\times 20$ lens both in air and water. This roughly agrees with the expectation from the four times difference in ℓ_f [see Eq. (12)]. With the UHF cantilever, the $\times 5$ lens still gives a lower n_z but the factor of the difference is reduced to 1.5–1.8 due to the laser power loss caused by the excessive laser spot size. While n_z obtained with the $\times 20$ lens continuously decreases with decreasing ℓ_c as expected from Eq. (12), the $\times 5$ lens gives a higher n_z for the UHF cantilever than that for the NCVH cantilever. Therefore, it is likely that the $\times 20$ lens will give a better performance than the $\times 5$ lens when the cantilever dimension is further reduced.

The resonance frequency of the UHF cantilever in air is so high (about 1.6 MHz) that the noise performance is partially limited by the insufficient bandwidth of the photodetector and the differential amplifier. Thus, increasing the

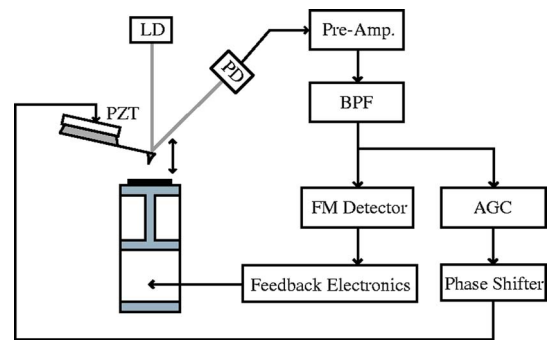


FIG. 10. (Color online) Experimental setup for the developed FM-AFM with the low noise deflection sensor.

bandwidth of those circuits may further improve the noise performance obtained with the high frequency cantilevers.

V. FM-AFM IMAGING

Figure 10 shows the experimental setup for the developed FM-AFM apparatus with the low noise deflection sensor. The circuit designs for the preamplifier and the bandpass filter (BPF) have been described previously.⁹ The deflection signal output from the BPF is fed into an FM detector (Nanosurf: EasyPLL Plus). The frequency shift signal from the FM detector is fed into the feedback electronics (Asylum Research: MFP-3D Controller) which controls the high voltage signal applied to the custom made piezotube scanner. The deflection signal is also routed to the home-built self-excitation circuit consisting of an automatic gain control (AGC) circuit and a phase shifter. The cantilever is excited with a piezoactuator in constant amplitude mode, where the excitation voltage is adjusted to keep the oscillation amplitude (A) constant. The tip-sample distance regulation was

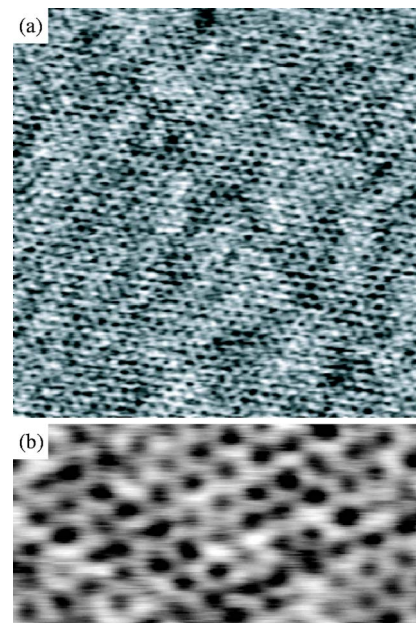


FIG. 11. (Color online) FM-AFM images of mica taken in water. (a) $20 \times 20 \text{ nm}^2$, scanning speed: 586 nm/s , $\Delta f = +300 \text{ Hz}$, $A = 0.55 \text{ nm}$. (b) $6.6 \times 3.3 \text{ nm}^2$, scanning speed: 732 nm/s , $\Delta f = +644 \text{ Hz}$, $A = 0.58 \text{ nm}$. The cantilever used was NCHR from Nanosensors. The $\times 5$ lens was used.

made in constant frequency shift mode, where the resonance frequency shift (Δf) is kept constant by controlling the vertical position of the sample.

Figure 11 shows the FM-AFM images of mica taken in water. The mica substrate was freshly cleaved in air and immersed in pure water immediately after the cleavage. Figure 11(a) shows a honeycomblike structure which is characteristic of the atomic structure of the mica surface. The period of the structure is about 0.52 nm. A more magnified image shown in Fig. 11(b) shows some atomic-scale bright spots as well as the underlying honeycomblike pattern. The bright spots are previously attributed to Al^{3+} ions consisting of the honeycomblike lattice⁸ although there still remains other possibilities such as K^+ ions. The imaging ability of such irregular atomic-scale features demonstrates the true atomic resolution of the developed FM-AFM.

ACKNOWLEDGMENT

This research was supported by Science Foundation Ireland Research Grant (01/PI.2/C033).

- ¹T. R. Albrecht, P. Grütter, D. Horne, and D. Rugar, *J. Appl. Phys.* **69**, 668 (1991).
- ²F. J. Giessibl, *Science* **267**, 68 (1995).
- ³S. Kitamura and M. Iwatsuki, *Jpn. J. Appl. Phys., Part 2* **34**, L1086 (1995).
- ⁴S. P. Jarvis, T. Uchihashi, T. Ishida, H. Tokumoto, and Y. Nakayama, *J. Phys. Chem. B* **104**, 6091 (2000).
- ⁵S. P. Jarvis, T. Ishida, T. Uchihashi, Y. Nakayama, and H. Tokumoto, *Appl. Phys. A: Mater. Sci. Process.* **72**, S129 (2001).
- ⁶T. Fukuma, T. Ichii, K. Kobayashi, H. Yamada, and K. Matsushige, *Appl. Phys. Lett.* **86**, 034103 (2005).
- ⁷T. Fukuma, K. Kobayashi, K. Matsushige, and H. Yamada, *Appl. Phys. Lett.* **86**, 193108 (2005).
- ⁸T. Fukuma, K. Kobayashi, K. Matsushige, and H. Yamada, *Appl. Phys. Lett.* **87**, 034101 (2005).
- ⁹T. Fukuma, M. Kimura, K. Kobayashi, K. Matsushige, and H. Yamada, *Rev. Sci. Instrum.* **76**, 053704 (2005).
- ¹⁰*Noncontact Atomic Force Microscopy (Nanoscience and Technology)*, edited by S. Morita, R. Wiesendanger, and E. Meyer (Springer-Verlag, New York, 2002).
- ¹¹F. J. Giessibl, H. Bielefeldt, S. Hembacher, and J. Mannhart, *Appl. Surf. Sci.* **140**, 352 (1999).
- ¹²F. J. Giessibl, *Appl. Phys. Lett.* **76**, 1470 (2000).
- ¹³F. J. Giessibl, S. Hembacher, H. Bielefeldt, and J. Mannhart, *Science* **289**, 422 (2000).
- ¹⁴G. T. Paloczi, B. L. Smith, P. K. Hansma, and D. A. Walters, *Appl. Phys. Lett.* **73**, 1658 (1998).
- ¹⁵S. Hosaka, K. Etoh, A. Kikukawa, and H. Koyanagi, *J. Vac. Sci. Technol. B* **18**, 94 (1999).
- ¹⁶T. Ando, N. Kodera, E. Takai, D. Maruyama, K. Saito, and A. Toda, *Proc. Natl. Acad. Sci. U.S.A.* **98**, 12468 (2001).
- ¹⁷H. Kawakatsu, S. Kawai, D. Saya, M. Nagashio, D. Kobayashi, and H. Toshiyoshi, *Rev. Sci. Instrum.* **73**, 2317 (2002).
- ¹⁸T. Fukuma, K. Kimura, K. Kobayashi, H. Yamada, and K. Matsushige, *Appl. Phys. Lett.* **85**, 6287 (2004).
- ¹⁹B. W. Hoogenboom *et al.*, *Appl. Phys. Lett.* **86**, 074101 (2005).
- ²⁰Y. Martin, C. C. Williams, and H. K. Wickramasinghe, *J. Appl. Phys.* **61**, 4723 (1987).
- ²¹D. Sarid, *Scanning Force Microscopy with Applications to Electric, Magnetic and Atomic Forces* (Oxford University Press, New York, 1994).
- ²²R. Proksch, T. E. Schäffer, J. P. Cleveland, R. C. Callahan, and M. B. Viani, *Nanotechnology* **15**, 1344 (2004).